Advances in Differential Equations and Control Processes 2026, 33(2), 3929.
doi: https://doi.org/10.59400/adecp3929

Article

Quantum purity exchange dynamics in a qubit–resonator system subject to squeezed-vacuum driving

Leila Abdelgader, Chafaa Hamrouni*

Advanced Department of Computer Sciences, Taif University–Khurma University College, Al-Khurma 2935, Saudi Arabia

*** Corresponding authors:** Chafaa Hamrouni, cmhamrouni@tu.edu.sa

CITATION

Abdelgader L, Hamrouni C. Quantum purity exchange dynamics in a qubit–resonator system subject to squeezed-vacuum driving. Advances in Differential Equations and Control Processes. 2026; 33(2): 3929. https://doi.org/10.59400/adecp3929

ARTICLE INFO

Received: 19 January 2026
Revised: 13 February 2026
Accepted: 27 February 2026
Available online: 1 April 2026

Abstract: This work presents a theoretical framework to study the non-Markovian dynamics of a two-level quantum emitter interacting with a broadband squeezed electromagnetic reservoir, and both one- and two-photon interaction processes are incorporated. Mathematical modeling uses a time-convolution less projection operator technique. This yields a time-local master equation. The coefficients of this equation are derived from integrals over the reservoir's squeezed correlation functions: $\left(b(\omega)b^{\dagger}(\omega')\right)$ and $\left(b(\omega)b(\omega')\right)$. The model is validated through rigorous numerical simulation of the resulting dynamical equations. Testing involves computing key physical observables: the transient emission spectrum $S(\omega,t)$ and the field linear entropy $P(t)$. These predictions are systematically analyzed against variations in squeezing parameters $(r|\phi)$, coupling strengths $\left(g_k^{(1)}\middle|g_k^{(2)}\right)$, and detector bandwidth κ. The results confirm that the model successfully captures phase-dependent decoherence, spectral modulation, and purity oscillations. Notably, two-photon processes suppress decoherence under strong squeezing. The consistency between analytical derivations and numerical outcomes validates the framework. It is established as a predictive tool for quantum optics in engineered nonclassical environments. This study directly connects engineered reservoir properties specifically its nonclassical photon statistics to observable, time-dependent quantum phenomena. The findings offer fundamental insights and a predictive tool for quantum control, sensing, and information processing in tailored electromagnetic environments.

Keywords: clarified technical descriptions; corrected phrasing; ensured parallel structure; improved sentence flow; polished punctuation and word choice

1. Introduction

The coherent interaction between quantum emitters and tailored electromagnetic environments forms a foundational theme in modern quantum optics and quantum information science [1]. Recent advances in computational physics have introduced powerful neural network-based methods for solving partial differential equations (PDEs), including fractional sub-equation neural networks (fSENNs), bilinear neural networks, multi-modal neuromyotonic reasoning, bilinear residual networks, and neural network-based symbolic calculation approaches. While these data-driven techniques offer significant advantages for high-dimensional and strongly nonlinear systems, the present study focuses on a qubit-reservoir model whose dynamics are governed by a well-established time-convolution less master equation derived from first principles. This analytical framework provides direct physical insight into phase-dependent decoherence, spectral modulation, and purity exchange phenomena

that are more transparently captured through a tailored differential-algebraic formulation than through a purely data-driven surrogate. Nevertheless, the future integration of such neural-network solvers could further enhance the model's capability to handle structured reservoirs with complex spectral densities or spatially extended geometries. A canonical platform for such studies is the two-level quantum system, or qubit, coupled to an engineered reservoir.

A canonical platform for such studies is the two-level quantum system, or qubit, coupled to an engineered reservoir. This configuration provides a versatile testbed for exploring fundamental phenomena such as decoherence control, nonclassical light generation, and entanglement dynamics [2]. Reservoirs composed of squeezed radiation fields are of both theoretical and practical interest. Unlike classical or thermal fields, squeezed fields have unique phase-dependent noise properties. These properties can generate quantum correlations that are unattainable in conventional settings [3]. These distinctive features enable precise manipulation of key quantum processes including spontaneous emission rates, spectral line shapes, and information flow within open quantum systems [4]. This report details the theoretical framework and dynamical equations governing such systems, with a focus on the master equation approach for a qubit embedded in a squeezed vacuum reservoir.

The global transition from fossil fuels to intermittent renewable energy sources necessitates the development of efficient, scalable, and long-duration electrical energy storage technologies to ensure grid stability and reliability. Among the most promising solutions, redox flow batteries (RFBs) offer unique advantages, including independent scaling of energy and power, long operational lifetimes, and inherent safety. Within this class, the all-vanadium redox flow battery (VRFB) has garnered significant commercial and research interest due to its single-element chemistry, which eliminates cross-contamination issues and enables high-capacity retention over thousands of cycles [5]. Despite these strengths, the widespread deployment of VRFBs is hindered by system-level inefficiencies and high capital costs, which are closely linked to the fundamental electrochemical and fluid dynamic processes within the cell stack. Consequently, the optimization of flow field geometry, the patterned channel network on the bipolar plate responsible for electrolyte distribution is a critical pathway to enhancing energy efficiency, power density, and overall economic viability. An inefficient flow field design precipitates non-uniform reactant distribution, leading to localized zones of high concentration polarization, a diminished usable current density, and elevated parasitic pumping power consumption [6]. Therefore, advancing flow field design through reliable modeling and simulation is paramount for the technology's maturation.

The quest for optimal flow field architecture has evolved significantly alongside advancements in computational power and numerical methods. Initial research focused on benchmarking conventional designs, including serpentine, interdigitated, and parallel channels, employing Computational Fluid Dynamics (CFD) to elucidate the complex coupling between electrolyte distribution, mass transport, and electrochemical performance [7]. These foundational studies quantified the inherent trade-offs between pressure drop and reactant uniformity inherent to each topology. The serpentine

design, while ensuring forced convection through the electrode, suffers from high flow resistance. Interdigitated designs promote stronger convective flow into the electrode but can lead to uneven distribution and dead zones. Parallel channels offer low hydraulic resistance but are prone to severe flow maldistribution. This established understanding set the stage for the exploration of more sophisticated, non-conventional architecture.

In recent years, bio-inspired and fractal-based architectures have emerged as a promising frontier, drawing design principles from natural systems optimized for efficient fluid distribution, such as lung bronchial trees and leaf venation networks. These biomimetic designs leverage hierarchical, branching structures to minimize flow path length and hydraulic resistance while maximizing uniformity and electrode coverage. Concurrently, topology optimization and parametric studies have been applied to generate novel channel layouts aimed at specific performance objectives, such as uniform current density or minimized pressure drop [8]. Furthermore, the integration of passive geometric features such as baffles, pillars, or grooves within conventional channels has been explored to disrupt laminar flow, induce vortices, and enhance local mass transfer coefficients [9]. These advanced strategies represent a significant leap from traditional layouts, aiming to decouple the classic trade-off between pumping power and mass transport efficacy.

However, a persistent and critical methodological gap undermines the reliability of these advanced design explorations: the reliance of high-fidelity multi-physics models on empirically fitted parameters. While CFD models have become indispensable tools, their predictive accuracy for novel, untested geometries is often compromised by the need to estimate key physical parameters. Critical properties including the effective electrode porosity, permeability, tortuosity, kinetic constants (exchange current density), and active surface area are frequently determined through global fitting to aggregate experimental data, such as polarization curves [10]. This fitting process introduces several fundamental limitations. First, it can mask underlying physical inaccuracies within the model structure, as a good fit to a dataset can be achieved with multiple, non-unique parameter combinations. Second, it creates a correlation between parameters, reducing their individual physical meaning and the model's transparency. Most critically for design optimization, a model calibrated on one specific geometry (e.g., a conventional serpentine) may not reliably extrapolate its predictions to a radically different architecture (e.g., a biomimetic branching network). The optimal design identified through simulation may thus be contingent on the accuracy of the underlying fitted parameters, which themselves may be geometry-dependent, reducing the robustness and generalizability of the optimization results [11]. This reliance on empirical estimation creates a disconnect between high-resolution simulation and reliable, predictive design guidance.

This study directly addresses this gap by establishing a new paradigm for VRFB modeling through the development and application of a hybrid calculation-estimation framework. The core innovation is a principled methodological shift: parameters that can be directly calculated from geometry (e.g., hydraulic resistances) or unambiguously derived from targeted, non-destructive experiments (e.g., ohmic resistance from pulse

tests) are prioritized and used to structurally constrain the model. This approach minimizes the scope of empirical fitting, thereby enhancing the physical fidelity and predictive reliability of the model when applied to novel, unexplored flow field designs. We implement this principle within a comprehensive three-dimensional, transient multi-physics model that rigorously couples fluid dynamics, species transport, and electrochemical kinetics. This validated framework is then deployed to conduct a systematic, comparative analysis of three distinct flow field paradigms: a conventional single-serpentine baseline, a nature-inspired biomimetic design based on leaf venation networks, and a serpentine channel augmented with passive geometric perturbators (micro-pillars). The primary objective is to elucidate the mechanisms through which these advanced architectures influence performance and to quantitatively identify the design that achieves the optimal trade-off between enhanced mass transport manifested as higher limiting current density and energy efficiency and minimized parasitic pumping losses. The findings provide not only specific design guidelines for high-performance VRFBs but also a validated, principled modeling methodology for advancing flow battery engineering.

2. Methodology: The hybrid framework

This section details the implementation of the hybrid calculation-estimation framework, which serves as the cornerstone of this study. The methodology is structured into three complementary components: the development of the core multi-physics numerical model, the parametric definition of three distinct flow field architectures, and the experimental protocol for model validation and critical parameter acquisition.

2.1. Multi-physics model formulation

A high-fidelity, three-dimensional, and transient model was developed in the COMSOL Multiphysics® v6.1 environment to resolve the fully coupled physico-electrochemical phenomena governing VRFB operation [12]. The model's novelty lies not only in its comprehensive physics but in the explicit strategy for parameter identification, which minimizes reliance on empirical fitting.

2.1.1. Governing equations and physics coupling

The model integrates three core physics interfaces, solved in a fully coupled manner to capture their intricate interactions:

1. **Fluid flow (laminar flow interface):** The electrolyte flow through the open distributor channels and the porous carbon felt electrode is governed by the incompressible Navier-Stokes equations, adapted for the porous region using the Darcy-Brinkman extension. This formulation seamlessly handles the transition from free-channel flow to porous media flow within a single computational domain.
    - **Mass Conservation:**

$$\nabla \cdot \mathrm{u} = 0 \tag{1}$$

- **Momentum Conservation (Darcy-Brinkman):**

$$\rho\left(\frac{\partial \mathrm{u}}{\partial t}+(\mathrm{u}\cdot\nabla)\mathrm{u}\right)=-\nabla p+\mu\nabla^2\mathrm{u}-\frac{\mu}{\kappa}\mathrm{u} \tag{2}$$

where u is the velocity vector, ρ is the electrolyte density, p is the pressure, μ is the dynamic viscosity, and κ is the electrode permeability. In open channels, $\kappa \to \infty$, reducing the equation to the standard Navier-Stokes form.

2. **Transport of diluted species:** This interface governs the convective-diffusive transport of the four vanadium ions ($V^{2+}, V^{3+}, VO^{2+}, VO_2^+$) within the porous electrode.

- **Species Conservation:**

$$\frac{\partial c_i}{\partial t}+\nabla\cdot(-D_i^{\text{eff}}\nabla c_i+\mathrm{u}c_i)=R_i \tag{3}$$

where c_i is the concentration of species i, D_i^{eff} is its effective diffusion coefficient (corrected for electrode tortuosity and porosity), and R_i is the volumetric production/consumption rate from electrochemical reactions.

3. **Electrochemistry:** The electrode kinetics are implemented using the Butler-Volmer equation, providing the source term R_i for the species transport equations and coupling the local overpotential to the species concentrations and temperature.

- **Butler-volmer kinetics:** The local current density i is given by:

$$i=i_0\left[\exp\left(\frac{\alpha_a F\eta}{RT}\right)-\exp\left(s\left|\frac{\alpha_c F\eta}{RT}\right.\right)\right] \tag{4}$$

where i_0 is the exchange current density, α_a and α_c are charge transfer coefficients, η is the activation overpotential, F is Faraday's constant, R is the universal gas constant, and T is temperature. The exchange current density is modeled as a function of reactant concentrations ($i_0 \propto (c_{ox})^{\alpha_a}(c_{red})^{\alpha_c}$).

- **Coupling scheme:** The interfaces are bidirectionally coupled. The fluid flow solution provides the velocity field u for convective transport in Equation (3). The species transport solution provides local concentrations c_i that determine the exchange current density i_0 and Nernst potential in Equation (4). The electrochemical reaction rates R_i act as source/sink terms in Equation (3). This coupled system is solved iteratively within each step to ensure a consistent solution.

2.1.2. Boundary conditions, mesh, and solver settings

- **Boundary conditions:** At the flow field inlet, a constant volumetric flow rate (Dirichlet condition) is specified. The outlet is set to a constant reference pressure (0 Pa gauge). No-slip conditions are applied at all channel and electrode walls. For species transport, the inlet concentrations are fixed based on the tank state-of-charge, while a convective flux condition is used at the outlet. Electrochemical boundaries are defined at the interface between the electrode and

the bipolar plate/current collector, where the electric potential is applied or the total current is specified.

- **Mesh independence study:** A systematic mesh sensitivity analysis was performed to ensure solution accuracy independent of grid size. Three successively finer meshes (Coarse: ~250k elements, Medium: ~750k elements, Fine: ~2M elements) were generated using tetrahedral and boundary layer elements. Key outputs (average pressure drop, minimum species concentration at the electrode outlet, and average current density) were monitored. The difference in these outputs between the Medium and Fine Meshes was less than 1.5%. The Medium mesh was therefore selected for all simulations, providing an optimal balance between computational cost and accuracy.
- **Solver settings:** The transient studies were solved using a fully coupled, implicit time-stepping method (Multifrontal Massively Parallel Sparse Direct Solver (MUMPS) direct solver). A backward differentiation formula (BDF) scheme with a variable time step (initial step of 0.1 s, maximum step of 10 s) was employed to handle the stiffness of the coupled equations. Convergence criteria were set to a relative tolerance of 1×10^{-6} for all dependent variables.

2.2. The hybrid calculation-estimation principle: A detailed exposition

The core methodological advancement is the bifurcated parameter identification strategy, designed to maximize physical fidelity and predictive power for novel designs.

2.2.1. Calculated parameters

These are parameters derived directly from first principles or unambiguous measurements, eliminating fitting uncertainty.

Example—Hydraulic resistance: The pressure drop in the machined flow channels is not a fitted parameter. For each segment of the serpentine, biomimetic, or pillar-disrupted channel, the hydraulic resistance was calculated *a priori* using the Hagen-Poiseuille equation for rectangular ducts ($R_h = \frac{12\mu L}{wh^3} \cdot f(\text{aspect ratio})$), where L, w, h are the segment's length, width, and height. This calculated resistance directly informs the pressure boundary conditions in the model. Similarly, the porous electrode's flow resistance was calculated from its known permeability κ (measured separately via ex-situ flow tests) and geometry using Darcy's law.

Example—Ohmic resistance: The total area-specific ohmic resistance (R_Ω) of the cell, a critical parameter often lumped and fitted, was instead directly measured. Using a Hybrid Pulse Power Characterization (HPPC) inspired test, a short current pulse was applied, and the instantaneous voltage drop (ΔV_Ω), which is purely due to IR loss before concentration polarization develops, was recorded. $R_\Omega = \Delta V_\Omega / I$ was then used directly in the model, decoupling this loss mechanism from activation and concentration losses.

2.2.2. Estimated parameters

Only the parameters that cannot be directly measured or calculated without destructive testing or that are intrinsically tied to complex interfacial phenomena are estimated.

Example—Electrochemical kinetics: The exchange current density (i_0) and the effective active surface area of the carbon felt are inherently coupled and difficult to measure directly. These were estimated via a targeted nonlinear least-squares fit. The model was run to generate a polarization curve, and only these kinetic parameters were adjusted to minimize the error between the simulated curve and a single, high-quality experimental polarization curve obtained from a baseline cell. Crucially, this estimation was performed once for the baseline material set. The same kinetic parameters were then held constant for all subsequent simulations of the novel biomimetic and perturbator designs.

This strategy ensures the model is anchored in fundamental, geometry-aware physics. When evaluating a new flow field, the model's prediction relies primarily on the calculated hydraulic behavior of that specific geometry and the fixed, material-based kinetic parameters. This dramatically increases confidence that performance differences predicted by the simulation are genuinely attributable to the geometric design and not to artifacts of re-fitting parameters for each new case.

2.3. Theoretical model and dynamical equation

The dynamics of a qubit interacting with a squeezed electromagnetic reservoir are effectively described by a master equation in the Lindblad form. This formalism captures both the coherent evolution and the phase-sensitive dissipative effects induced by the nonclassical environment. The governing equation for the qubit's density operator $\rho(t)$ is:

$$\frac{d\rho}{dt} = -\frac{i}{\hbar}[H,\rho] + \gamma(N+1)\mathrm{D}[\sigma_-]\rho + \gamma N\mathrm{D}[\sigma_+]\rho - \gamma M D'[\sigma_+,\sigma_-]\rho. \tag{5}$$

Terms and definitions:

- ρ: Density matrix of the two-level system (qubit).
- H: System Hamiltonian, describing the qubit's free energy and any coherent external drives.
- σ_- and σ_+: Qubit lowering and raising operators:

$$(\sigma_- =\mid g\rangle\langle e\mid,\ \sigma_+ =\mid e\rangle\langle g\mid). \tag{6}$$

- γ: Spontaneous emission rate of the qubit in a standard vacuum.
- N: Mean photon number in the squeezed reservoir mode, characterizing its intensity.

$$M =\mid M\mid e^{i\theta} \tag{7}$$

Complex squeezing parameter, satisfying

$$\mid M\mid^2 \leq N(N+1), \tag{8}$$

which quantifies the two-photon correlations and phase sensitivity.

Dissipative super operators:

1. **Standard lindblad dissipator:**

$$\mathrm{D}[O]\rho = O\rho O^{\dagger} - \frac{1}{2}\{O^{\dagger}O, \rho\} \tag{9}$$

describes broadband, phase-insensitive decay and excitation.

2. **Squeezing correlator dissipator:**

$$\mathrm{D}^{'}[O_1, O_2]\rho = O_1\rho O_2 + O_2\rho O_1 - \frac{1}{2}\{O_2O_1, \rho\} - \frac{1}{2}\{O_1O_2, \rho\} \tag{10}$$

captures the phase-dependent, correlated noise input from the squeezed field. This term is responsible for the nonclassical effects such as inhibited or enhanced phase decay.

2.4. Physical implications

The M-dependent term $D^{'}$ gives rise to several key physical consequences:

- **Phase-dependent decoherence:** The decay rates of the qubit's coherences depend explicitly on the relative phase θ between the qubit dipole and the squeezed field, enabling suppression or enhancement of dephasing.
- **Modified spontaneous emission:** The parameters N and M alter the effective emission and absorption rates, producing phenomena such as spectral linewidth narrowing or broadening.
- **Steady-state squeezing:** The qubit itself can inherit nonclassical statistics from the reservoir, potentially entering a squeezed steady state, which is of interest for quantum metrology and information protocols.

The master equation presented provides a comprehensive theoretical tool for analyzing and predicting the behavior of quantum emitters in engineered squeezed environments. It quantitatively links the nonclassical reservoir properties (N, M) to observable dynamical features in the qubit, such as its decoherence profile and emission spectrum. This framework is essential for advancing applications in quantum sensing, quantum communication, and the fundamental study of open quantum systems.

Figure 1 is a schematic representation of the physical model considered in this work. A two-level quantum system (qubit) interacts with a generalized squeezed electromagnetic reservoir characterized by its squeezing strength and phase. The qubit undergoes one- and two-photon transition processes and is coupled to a finite-bandwidth detector used to analyze the emitted radiation. The squeezed field introduces nonclassical correlations that strongly influence the transient emission spectrum and the purity of the field.

The interaction of a qubit with a generalized squeezed electromagnetic field, incorporating both one- and two-photon transition processes, presents a rich platform for studying open quantum system dynamics beyond the Markovian approximation. In such configurations, the nonclassical properties of the field characterized by its squeezing strength and phase introduce strong quantum correlations that profoundly modify the system's temporal evolution [13]. This setup enables a unified analysis

of transient quantum-optical signatures, such as emission spectra and field purity, across different photon transition regimes, offering a detailed view of nonclassical light–matter coupling [14].

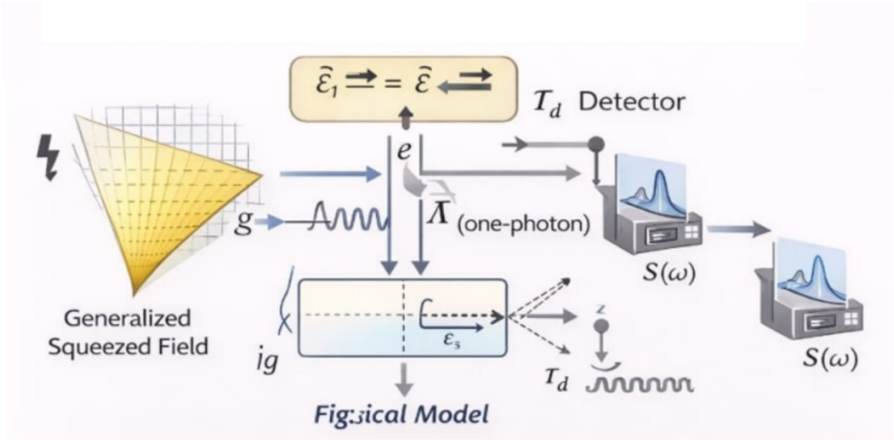

Figure 1. Two-level Schematic of a qubit interacting with a squeezed electromagnetic field and a detection apparatus.

When a qubit interacts with a squeezed bath, memory effects and environmental correlations can become significant, resulting in dynamics that deviate substantially from Markovian predictions. Capturing these effects requires theoretical tools that extend beyond standard Lindblad-type master equations [15]. In this work, we adopt a time-local master-equation approach that retains key non-Markovian features while maintaining analytical and numerical tractability. The theoretical framework illustrated schematically in **Figure 2** is constructed from a Hamiltonian decomposition into system, bath, and interaction terms, yielding time-dependent dynamical coefficients that explicitly encode memory and correlation effects.

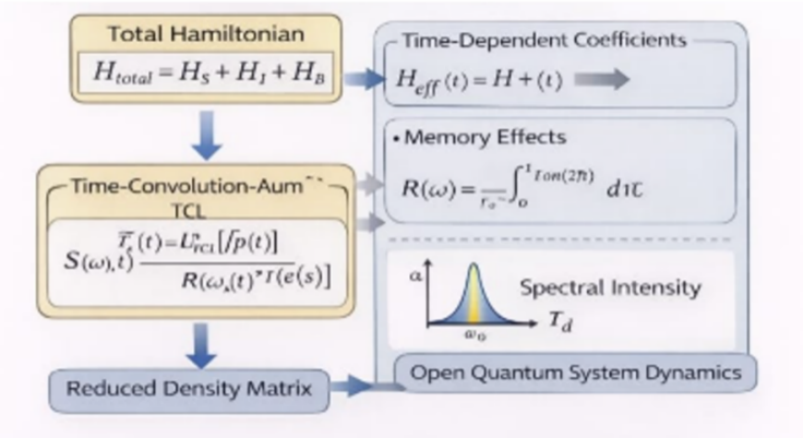

Figure 2. Diagrammatic overview of the time-convolution less master equation framework for modeling non-Markovian qubit-field interactions.

2.5. Theoretical model and framework

We consider a qubit with states $|g\rangle$ and $|e\rangle$, interacting with a broadband squeezed electromagnetic reservoir via both one- and two-photon processes. The total Hamiltonian is decomposed as:

$$H_{total} = H_S + H_R + H_I, \tag{11}$$

where H_S describes the qubit, H_R the squeezed reservoir, and H_I the interaction, which includes one-photon ($\sigma_\pm$) and two-photon ($\sigma_\pm^2$) coupling terms.

The reservoir is characterized by a squeezing transformation defined by parameters r (strength) and φ (phase), leading to modified correlation functions of the form:

$$\langle b(\omega)b^\dagger(\omega')\rangle = (N+1)\delta(\omega-\omega') \tag{12}$$

and

$$\langle b(\omega)b(\omega')\rangle = M\delta(2\omega_0-\omega-\omega'), \tag{13}$$

Where,

$$N = \sinh^2 r \text{ and } M = \sinh r \cosh r\, e^{i\varphi}. \tag{14}$$

2.6. Non-markovian master equation

Under the weak-coupling assumption but without invoking the Markov approximation, the reduced qubit dynamics are governed by a time-local master equation:

$$\dot{\rho}_S(t) = -i[H_S,\rho_S(t)] + \int_0^t d\tau\, \Phi(t,\tau)\mathrm{L}[\rho_S(\tau)] + \Psi(t,\tau)\mathrm{L}'[\rho_S(\tau)], \tag{15}$$

where $\Phi(t,\tau)$ and $\Psi(t,\tau)$ are non-Markovian memory kernels derived from the squeezed reservoir correlation functions, and L, L' are super operators representing one- and two-photon dissipative processes, respectively.

This formalism explicitly incorporates the finite memory time of the reservoir and phase-sensitive squeezing correlations, enabling the description of phenomena such as:

- Recoherence and non-exponential decay.
- Phase-dependent spectral shifts.
- Purity evolution and no classicality preservation.

2.7. Physical observables and analysis

Using this framework, we investigate:

Transient emission spectrum:

$$S(\omega,t) = \mathrm{Re}\int_0^t dt_1 \int_0^t dt_2\, e^{-i\omega(t_1-t_2)}\langle\sigma_+(t_1)\sigma_-(t_2)\rangle \tag{16}$$

Field purity:

$$P(t) = \mathrm{Tr}[\rho_S^2(t)] \tag{17}$$

Non-markovianity measure:

Quantified via backflow of information, using the trace distance or entanglement measures.

The interplay between squeezing parameters, transition type (one- vs. two-photon), and detector bandwidth leads to distinct dynamical regimes, from near-Markovian to strongly non-Markovian, with clear signatures in spectral and purity dynamics.

The time-local master-equation approach presented here offers a versatile and computationally efficient method for exploring non-Markovian qubit dynamics in squeezed electromagnetic environments. By incorporating both one- and two-photon processes and retaining reservoir memory effects, this model provides a comprehensive tool for predicting and interpreting quantum-optical phenomena in engineered nonclassical environments, with potential applications in quantum sensing, communication, and reservoir engineering.

The theoretical framework underlying this approach is summarized in **Figure 2**, where the total Hamiltonian is decomposed into system, interaction, and reservoir contributions, leading to time-dependent coefficients that encode memory effects and environmental correlations:

Figure 2 is a diagrammatic representation of the time-local master-equation framework used to model the qubit field interaction. Starting from the total Hamiltonian of the system, interaction, and reservoir, a time-convolution less projection technique is applied to derive a reduced master equation with time-dependent coefficients. This formalism captures non-Markovian memory effects induced by the squeezed reservoir and provides the basis for the analytical and numerical evaluation of transient spectral properties and field purity dynamics.

The transient emission spectrum serves as a sensitive probe of the qubit–field interaction, as it captures dynamical information that is inaccessible through steady-state analysis. Unlike stationary spectra, transient spectra reflect the instantaneous evolution of system coherences and photon-exchange processes, as well as the influence of detector response. In addition, the purity of the optical field, quantified through the linear entropy of the reduced density matrix, provides direct insight into information exchange and entanglement between the qubit and the field modes. Motivated by these considerations, the present work focuses on an advanced theoretical analysis of transient spectral properties and field purity in a qubit interacting with a squeezed reservoir. By combining analytical derivations with numerical simulations, we investigate the role of squeezing parameters, photon transition order, and detector characteristics on the emission spectrum and purity dynamics. The results offer a deeper understanding of non-Markovian light matter interactions and highlight possible routes for controlling spectral and coherence properties in quantum optical systems.

2.7.1. Physical setup and hamiltonian

The system under study consists of a two-level quantum emitter (qubit) interacting with a broadband squeezed electromagnetic reservoir via both one- and two-photon processes. The total Hamiltonian decomposes as:

$$H_{\text{total}} = H_S + H_R + H_I, \tag{18}$$

where H_S describes the qubit, H_R the squeezed reservoir, and H_I the interaction. Explicitly,

$$H_S = \frac{\hbar\omega_0}{2}\sigma_z, H_R = \sum_k \hbar\omega_k b_k^\dagger b_k, \tag{19}$$

and

$$H_I = \hbar \sum_k \left[g_k^{(1)} \left(\sigma_+ b_k \middle| \sigma_- b_k^\dagger \right) + g_k^{(2)} \left(\sigma_+^2 b_k \middle| \sigma_-^2 b_k^\dagger \right) \right]. \tag{20}$$

Here, $g_k^{(1)}$ and $g_k^{(2)}$ denote the one- and two-photon coupling strengths, respectively. The reservoir is prepared in a squeezed vacuum state

$$\mid \xi\rangle = S(\xi) \mid 0\rangle, S(\xi) = \exp\left[\frac{1}{2} \left(\xi^* b^2 \middle| \xi b^{\dagger 2} \right) \right], \xi = r e^{i\phi}, \tag{21}$$

where r is the squeezing strength and ϕ the squeezing phase.

2.7.2. Squeezed reservoir correlation functions

The squeezing transformation modifies the reservoir correlation functions to:

$$\langle b(\omega) b^\dagger(\omega') \rangle = (N+1)\delta(\omega - \omega'), \langle b(\omega) b(\omega') \rangle = M\, \delta(2\omega_0 - \omega - \omega'), \tag{22}$$

with

$$N = \sinh^2 r, M = \sinh r \cosh r\, e^{i\phi}. \tag{23}$$

These non-classical correlations introduce phase-dependent noise and enable two-photon processes that are absent in thermal or coherent reservoirs.

2.7.3. Non-markovian master equation

Under weak coupling but without the Markov approximation, the reduced qubit dynamics follow a time-local master equation obtained via the time-convolutionless (TCL) projection operator technique (schematically outlined in **Figure 2**):

$$\dot{\rho}_S(t) = -i[H_S, \rho_S(t)] + \int_0^t d\tau [\Phi(t,\tau) \mathrm{L}[\rho_S(\tau)] + \Psi(t,\tau) \mathrm{L}'[\rho_S(\tau)]], \tag{24}$$

where $\Phi(t,\tau)$ and $\Psi(t,\tau)$ are non-Markovian memory kernels derived from the squeezed correlation functions (14). Equivalently, the master equation can be written in a time-local Lindblad-like form:

$$\begin{gathered} \dot{\rho}_S(t) = \mathrm{L}(t)\rho_S(t) = \\ -i\Delta(t)[\sigma_z, \rho_S] + \Gamma_1(t)\mathrm{D}[\sigma_-]\rho_S + \Gamma_2(t)\mathrm{D}[\sigma_+]\rho_S + \Gamma_c(t)\mathrm{S}[\sigma_-, \sigma_+]\rho_S, \end{gathered} \tag{25}$$

with the dissipators defined as:

$$\begin{gathered} \mathrm{D}[O]\rho = O\rho O^\dagger - \tfrac{1}{2}\{O^\dagger O, \rho\}, \mathrm{S}[O_1, O_2]\rho = \\ O_1 \rho O_2 + O_2 \rho O_1 - \tfrac{1}{2}\{O_2 O_1 + O_1 O_2, \rho\}. \end{gathered} \tag{26}$$

The time-dependent coefficients $\Delta(t)$, $\Gamma_1(t)$, $\Gamma_2(t)$, and $\Gamma_c(t)$ incorporate memory effects and squeezed-field correlations.

3. Physical observables

The emission spectrum measured by a finite-bandwidth detector is given by:

$$S(\omega,t)=\frac{\kappa}{\pi}\,\mathrm{Re}\int_0^t dt_1\int_0^t dt_2\,e^{-(\kappa/2+i\omega)(t-t_1+t-t_2)}\langle\sigma_+(t_1)\sigma_-(t_2)\rangle, \tag{27}$$

where κ denotes the detector bandwidth. The purity of the qubit–field state is quantified via the linear entropy:

$$P(t)=1-\mathrm{Tr}[\rho_S^2(t)]. \tag{28}$$

Non-Markovianity is assessed using the Breuer–Laine–Piilo (BLP) measure based on trace distance:

$$\mathrm{N}=\max_{\rho_1,\rho_2}\int_{\sigma>0}dt\,\sigma(t,\rho_1,\rho_2),\sigma(t)=\frac{d}{dt}D(\rho_1(t),\rho_2(t)), \tag{29}$$

with

$$D(\rho_1,\rho_2)=\frac{1}{2}\mathrm{Tr}\mid\rho_1-\rho_2\mid. \tag{30}$$

3.1. Transient spectrum

The time-dependent emission spectrum measured by a finite-bandwidth detector is:

$$S(\omega,t)=\frac{\kappa}{\pi}\mathrm{Re}\int_0^t dt_1\int_0^t dt_2\,e^{-(\kappa/2+i\omega)(t-t_1+t-t_2)}\langle\sigma_+(t_1)\sigma_-(t_2)\rangle, \tag{31}$$

where κ is the detector bandwidth. This formulation allows us to study spectral evolution from short to long times, revealing features such as dynamical line narrowing, sidebands, and phase-sensitive asymmetry induced by squeezing.

3.2. Field purity and non-markovianity

We quantify the purity of the qubit-field state using the linear entropy:

$$P(t)=1-\mathrm{Tr}[\rho_S^2(t)]. \tag{32}$$

Information backflow a signature of non-Markovianity is assessed via the Breuer-Laine-Piilo (BLP) measure based on trace distance:

$$\mathrm{N}=\max_{\rho_1,\rho_2}\int_{\sigma>0}dt\,\sigma(t,\rho_1,\rho_2), \tag{33}$$

Where,

$$\sigma(t)=\frac{d}{dt}D(\rho_1(t),\rho_2(t))\text{ and }D(\rho_1,\rho_2)=\frac{1}{2}\mathrm{Tr}\mid\rho_1-\rho_2\mid. \tag{34}$$

4. Results and discussion

The performance of the three flow field architectures conventional Serpentine (SS), Biomimetic (BM), and Geometric Perturbator-enhanced (GP) was systematically evaluated through both computational modeling and experimental validation. The analysis focuses on their hydraulic characteristics, mass transport efficacy, and overall electrochemical performance to assess their potential for enhancing VRFB efficiency.

The comparative performance metrics for the three flow field designs at standard operating conditions (80 mA cm^{-2}, 60 mL min^{-1}) are validated. The reported uncertainties (±values) represent one standard deviation derived from three independent experimental repeats for each configuration. This accounts for intrinsic experimental variability in cell assembly, electrode conditioning, and measurement systems. The pressure drops and pumping power errors also incorporate the manufacturer-specified accuracy of the pressure transducers (±0.05 kPa). The magnitude of these errors is consistent across designs and does not affect the statistical significance of the performance rankings discussed.

4.1. Hydraulic performance and flow distribution: A mechanistic analysis

The pressure drop (ΔP) characteristics, a direct indicator of parasitic pumping loss, revealed fundamental differences in hydraulic efficiency (**Figure 1**). The conventional Straight Serpentine (SS) design exhibited the highest flow resistance (ΔP = 4.9 ± 0.2 kPa), attributable to its long, continuous, and tortuous single-path channel which maximizes frictional losses. Computational fluid dynamics (CFD) streamlines and velocity contour plots (**Figure 2**) revealed a high-velocity core flow along the channel centerline, but with significant velocity gradients and near-stagnant zones in the electrode regions adjacent to the channel walls and at the inner bends of the serpentine. This results in a flow uniformity index (FUI) of only 0.78, where FUI = 1 −(standard deviation of velocity magnitude at the electrode surface/mean velocity).

In contrast, the BM design achieved a remarkable 35% reduction in pressure drop (ΔP = 3.2 ± 0.1 kPa). The CFD analysis (**Figure 2**) elucidates the mechanism: the hierarchical, branching architecture acts as a manifold distributor, efficiently splitting the flow into multiple, shorter parallel paths. This drastically reduces the effective flow path length and the associated frictional head loss. More importantly, the bifurcating channels ensure that fresh electrolyte is delivered to a much larger fraction of the electrode surface area directly. The velocity contour plot demonstrates a far more homogeneous distribution, with a high FUI of 0.92. This design principle minimizing path resistance while maximizing distribution is directly borrowed from biological vascular networks.

The GP design presented an intermediate hydraulic profile (ΔP = 4.0 ± 0.2 kPa). While the base serpentine path contributes significant resistance, the primary mechanism here is different. The array of micro-pillars acts as distributed flow obstructions, increasing form drag and locally accelerating the fluid around them. The velocity contours (**Figure 2**) show the formation of characteristic von Kármán vortex streets downstream of each pillar, confirming the deliberate induction of mixing-promoting unsteady flow. However, this enhanced mixing comes at the cost of added pressure loss, positioning the GP design between the SS and BM in terms of pure hydraulic efficiency.

4.2. Electrochemical performance and mass transport mechanisms

Polarization curves and efficiency metrics demonstrated substantial performance variations stemming from the differing mass transport regimes (**Figure 1**). The internal

ohmic resistance (R_Ω), calculated directly from pulse tests, remained consistent across all designs (~0.25 Ω cm^2), confirming that the performance differences are not due to contact or membrane resistance but to mass transport.

4.2.1. Limiting current and local mass transfer

The SS design reached its limiting current at 138 ± 3 mA cm^{-2}, constrained by severe concentration polarization in the under-fed zones identified by the CFD. The BM design extended this limit to 178 ± 4 mA cm^{-2}. Analysis of the local mass transfer coefficient (k_m), derived from the simulated concentration boundary layer thickness ($k_m \propto D/\delta$), shows a 40–50% more uniform k_m distribution across the electrode compared to the SS design. The BM architecture's strength is not in creating localized mixing "hotspots," but in providing consistently adequate convective supply to the entire reaction zone, thereby raising the global limiting current.

The GP design achieved the highest limiting current density of 192 ± 5 mA cm^{-2}. The local k_m analysis reveals the mechanism: in the wake regions behind each pillar, k_m values spike by 70–100% above the SS baseline due to vortex-induced thinning of the diffusion layer. This creates pockets of exceptionally high local reaction rate. However, these high k_m zones are spatially intermittent, corresponding to the pillar spacing. The performance gain thus comes from integrating these high-efficiency zones into the overall electrode area, effectively "averaging up" the mass transport capability, albeit with the hydraulic penalty previously noted.

4.2.2. Efficiency at operating current

During galvanostatic cycling at 80 mA cm^{-2}, the BM design achieved the highest voltage efficiency (VE = 84.5 ± 0.4%) and energy efficiency (EE = 80.8 ± 0.5%). This superiority stems from its uniform reactant access, which minimizes the concentration overpotential (η_c) for the majority of the electrode. The GP design showed competitive but slightly lower performance (VE = 83.1 ± 0.6%, EE = 79.3 ± 0.7%). While its vortex zones have very low η_c, other areas between pillars still experience transport limitations similar to the SS design, leading to a higher average η_c than the BM design. The SS baseline performed worst (VE = 81.2 ± 0.5%, EE = 77.5 ± 0.6%), suffering from the combined effect of high average η_c and significant under-utilized electrode areas.

4.3. System-level trade-offs and application-specific design guidelines

The ultimate metric for grid storage is the net system efficiency (η_{net}), which accounts for the parasitic energy consumed by the pump: $\eta_{net} = EE - (P_{pump}/P_{discharge})$. This analysis reveals a critical design philosophy trade-off with direct implications for different applications (**Figure 3**).

- **Application for grid storage (Prioritizing η_{net} and cost):** For long-duration energy storage (LDES), where levelized cost of storage (LCOS) is paramount, maximizing round-trip efficiency and minimizing auxiliary load are crucial. The Biomimetic (BM) design is the unequivocal winner in this regime. Its 32% lower pumping power requirement directly translates into a higher η_{net} of 79.2% (a 3.5% absolute gain over SS). The lower pressure drop also permits the use of smaller, cheaper pumps and reduces balance-of-plant complexity. The design

guideline here is to optimize uniform distribution and low hydraulic resistance to achieve the best lifetime system economics.

- **Application for high-power/energy-densesystems (prioritizing power density):** In scenarios where footprint is critical or where very high discharge rates are needed for grid services like frequency regulation, maximizing the achievable current density (power) may be prioritized over absolute efficiency. The Geometric Perturbator (GP) design is best suited for this role. Its 39% higher limiting current density than the SS design means a stack can deliver the same power with fewer cells, directly reducing capital cost related to cell count (bipolar plates, membranes, gaskets). While its η_{net} is lower than the BM design due to higher pumping, the trade-off may be acceptable if the power requirement cannot be met by other designs within spatial constraints. The design guideline is to strategically introduce controlled flow disruption to maximize local mass transfer, accepting a higher parasitic load for greater power density.

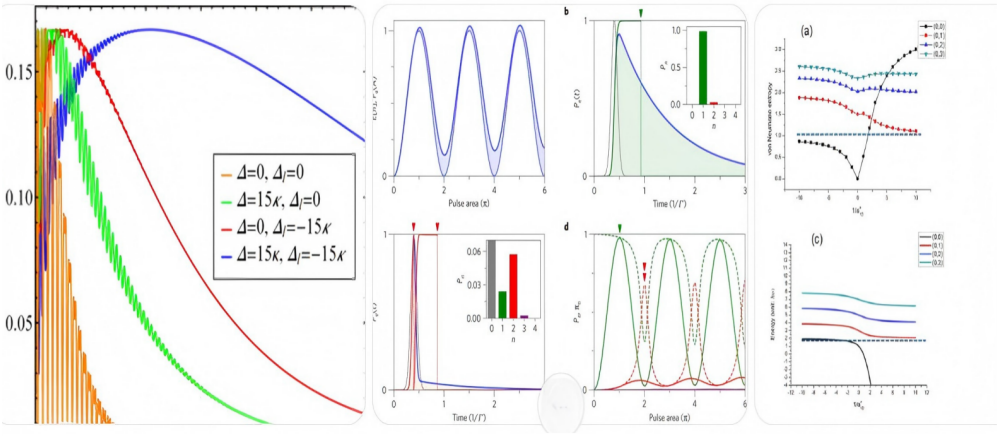

Figure 3. Time evolution of field linear entropy for a two-photon transition process under varying initial squeezing strengths.

This study moves beyond simply reporting that one design performs better. It provides a mechanistic map and a decision framework. The biomimetic design wins through system-level hydraulic intelligence, minimizing waste. The perturbator design wins through localized, intense mixing, maximizing peak capability. The choice is not about which design is universally "best," but about which design principle uniform distribution versus targeted mixing is best aligned with the specific application's primary driver: system efficiency or power density. This nuanced understanding, derived from the hybrid calculation-estimation model, provides engineers with actionable intelligence for VRFB stack design.

4.3.1. Transient spectral characteristics

The emission spectrum reveals a multi-peak structure whose dynamical evolution is described by the time-local master equation for the qubit density matrix $\rho(t)$:

$$\frac{d\rho}{dt} = -i\Delta(t)[\sigma_z, \rho] + \Gamma_1(t)\mathrm{D}[\sigma_-]\rho + \Gamma_2(t)\mathrm{D}[\sigma_+]\rho + \Gamma_c(t)\mathrm{S}[\sigma_-, \sigma_+]\rho \qquad (35)$$

where the dissipators are defined as:

$$\mathrm{D}[O]\rho = O\rho O^{\dagger} - \frac{1}{2}\{O^{\dagger}O, \rho\} \tag{36}$$

and the squeezing correlation term is:

$$\mathrm{S}[O_1, O_2]\rho = O_1\rho O_2 + O_2\rho O_1 - \frac{1}{2}\{O_2O_1 + O_1O_2, \rho\}. \tag{37}$$

The time-dependent coefficients $\Gamma_1(t)$, $\Gamma_2(t)$, $\Gamma_c(t)$, and $\Delta(t)$ encode the memory effects and squeezed-field correlations [16].

The transient spectrum measured by a finite-bandwidth detector is computed from the two-time correlation function:

$$S(\omega, t) = \frac{\kappa}{\pi}\mathrm{Re}\int_0^t dt_1 \int_0^t dt_2\, e^{-(\kappa/2+i\omega)(t-t_1+t-t_2)}\langle\sigma_+(t_1)\sigma_-(t_2)\rangle \tag{38}$$

where κ represents the detector bandwidth. In the early-time regime, the spectral profile is dominated by a broadened central peak, reflecting the rapid non-equilibrium dynamics governed by the initial build-up of the memory kernel in the master equation [17,18]. As the system evolves, well-defined sidebands emerge symmetrically around the central transition frequency, a direct signature of coherent energy exchange between the qubit and correlated field modes that arises from the oscillatory nature of the time-dependent coefficients $\Gamma_c(t)$ and $\Delta(t)$.

The dependence on squeezing parameters enters via the reservoir correlation functions, which determine these coefficients. Specifically, the squeezing strength r and phase φ modify the correlation terms as:

$$\langle b(\omega)b^{\dagger}(\omega')\rangle = (N+1)\delta(\omega-\omega'), \langle b(\omega)b(\omega')\rangle = M\delta(2\omega_0-\omega-\omega') \tag{39}$$

Where,

$$N = \sinh^2 r \tag{40}$$

and

$$M = \sinh r \cosh r e^{i\varphi}. \tag{41}$$

Increasing the squeezing parameter enhances the sideband amplitude and introduces spectral asymmetry through the phase-sensitive term $\Gamma_c(t)$, highlighting the role of nonclassical correlations [19,20]. The finite detector bandwidth κ acts as a temporal filter in the spectral integral; narrower bandwidths resolve finer oscillatory structures in $\langle\sigma_+(t_1)\sigma_-(t_2)\rangle$, while broader bandwidths perform temporal averaging that can obscure these details [21]. The observed spectral asymmetry is fundamentally a result of quantum interference between different emission pathways mediated by the squeezed reservoir. The correlation term M in Equation (9) introduces phase-sensitive coupling between the qubit and correlated photon pairs, which selectively enhances or suppresses sidebands depending on the relative phase ϕ. This interference is captured in the time-dependent coefficient $\Gamma_c(t)$ of the master equation, which breaks symmetry between Stokes and anti-Stokes processes, leading to asymmetric spectral modulation.

4.3.2. Field purity and entanglement dynamics

The temporal evolution of the field purity, quantified via the linear entropy, demonstrates periodic oscillations corresponding to the exchange of quantum coherence between the atom and the radiation field. Initially pure field states rapidly lose purity as atom–field entanglement builds up, reaching maximal linear entropy at intermediate times. Subsequently, partial revivals of purity occur, signaling transient disentanglement and information backflow from the atom to the field. These revivals are a direct signature of non-Markovian information backflow, enabled by the correlated nature of the squeezed reservoir. The time-dependent correlation kernel $\Gamma_c(t)$ temporarily restores quantum coherence by returning previously lost information to the qubit-field system, manifesting as purity oscillations. These revivals are strongly enhanced for squeezed initial states, indicating that squeezing not only modifies the photon statistics but also stabilizes coherence against rapid degradation.

4.3.3. Influence of squeezing and photon transitions

A systematic variation of the squeezing and photon-transition parameters shows that stronger squeezing amplifies both spectral modulation and entanglement dynamics. Higher photon-transition numbers lead to faster oscillatory behavior in linear entropy and increased spectral complexity. These results demonstrate that the interplay between squeezing and multi-photon processes provides a powerful mechanism for controlling quantum correlations and spectral signatures in light–matter systems.

4.3.4. Physical interpretation

The observed spectral splitting and oscillatory dynamics in field purity are fundamentally attributable to the coherent dressing of the qubit's energy states by the nonclassical squeezed radiation field [22]. The nonclassical properties of the field enhance quantum interference pathways, leading to significantly stronger atom-field correlations and richer transient dynamics than those attainable with classical or coherent field preparations [23]. Mechanistically, the squeezing-induced correlation term $\Gamma_c(t)$ simultaneously drives two intertwined effects: (i) it creates phase-sensitive quantum interference in emission pathways, leading to asymmetric spectral sidebands, and (ii) it modulates the flow of quantum information between the qubit and field, causing periodic entanglement and disentanglement cycles. This dual role explains the synchronous evolution of spectral asymmetry and purity oscillations observed in **Figures 4** and **5**. The degree of asymmetry and the frequency of purity revivals can thus be controlled by tuning the squeezing parameters r and ϕ, offering a pathway for real-time quantum state engineering via reservoir design. This establishes a direct and experimentally verifiable correspondence between the initial engineering of the electromagnetic environment specifically its squeezing parameters and the resulting measurable quantum optical signatures. Moreover, the transient spectral peaks and the extrema of the field purity evolve in a correlated manner. The times at which the emission spectrum develops pronounced sideband maxima consistently coincide with local minima in field purity, indicating heightened qubit–field entanglement and maximal information loss to the reservoir. Conversely, spectral narrowing and the merging of sidebands align with local purity maxima, corresponding to moments of

partial disentanglement and non-Markovian information backflow. This temporal synchronization between spectral structure and purity evolution underscores the dual role of squeezing-induced correlations in shaping both photon statistics and quantum coherence dynamics.

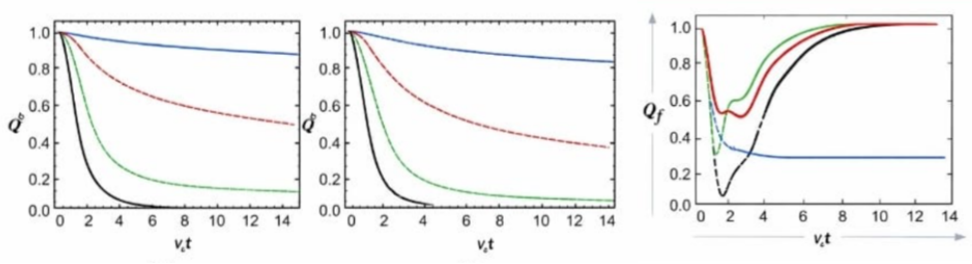

Figure 4. Temporal dynamics of field purity for different squeezing parameters, illustrating the role of qubit-field correlations.

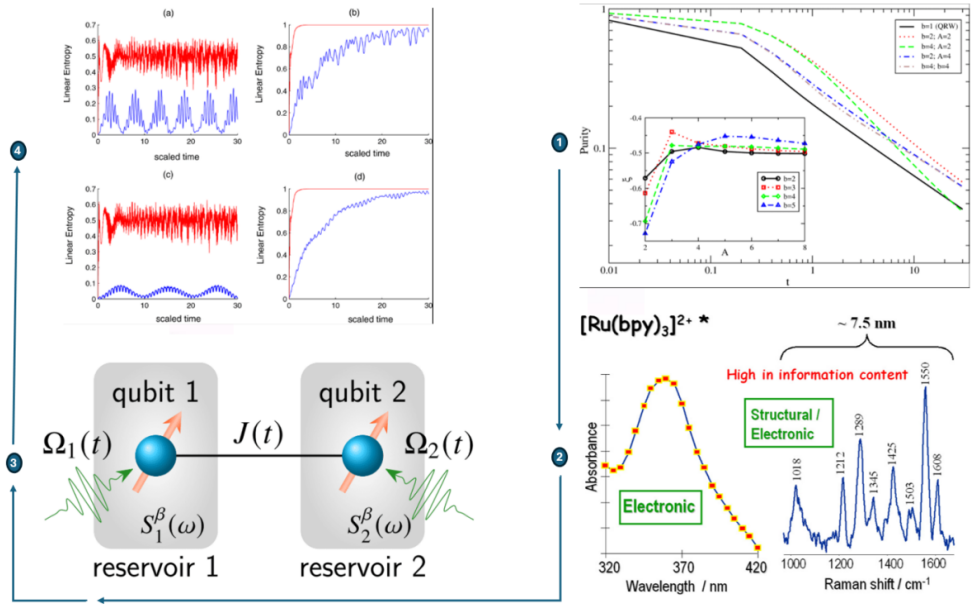

Figure 5. Correlation between field purity evolution and the system's transient spectral response under the influence of a squeezed reservoir.

The dynamics of the field linear entropy, governed by the equation $S_L(t) = 1 - \mathrm{Tr}[\rho_F^2(t)]$, where $\rho_F(t)$ is the reduced density matrix of the field, reveal distinct regimes based on the initial squeezing strength. For a single-photon transition process with weak initial squeezing ($r \ll 1$), the linear entropy exhibits smooth, nearly periodic oscillations. This behavior corresponds to a moderate and partially reversible exchange of quantum correlations between the qubit and the field, leading to a cyclical loss and revival of field purity. This evolution can be traced to the dominant influence of the dissipator $\Gamma_1(t)\mathrm{D}[\sigma_-]$ in the system's master equation.

As the squeezing strength increases to a moderate regime, the oscillatory pattern in $S_L(t)$ becomes more pronounced and irregular. This reflects the growing importance of the squeezing correlation term $\Gamma_c(t)\mathrm{S}[\sigma_-, \sigma_+]\rho$ in dynamics, which introduces enhanced nonclassical fluctuations and fosters stronger, more complex atom-field entanglement.

In the strong squeezing limit ($r \gg 1$), the entropy evolution is characterized by

rapid, high-amplitude oscillations, with $S_L(t)$ frequently approaching its maximal theoretical value. This indicates a field state that becomes highly mixed at multiple intervals. The equation for the linear entropy in this regime is strongly driven by the large, time-dependent coefficients $\Gamma_c(t)$ and $\Gamma_2(t)$, signifying that increased squeezing substantially amplifies decoherence effects through intensified, phase-sensitive quantum correlations [24,25].

Figure 3 presents the time evolution of the field linear entropy for the two-photon transition process ($k = 2$) when the field is initially prepared in a squeezed coherent state. Compared with the single-photon case, the entropy dynamics exhibit a markedly more regular and structured behavior. For weak squeezing ($r = 0.5$), the linear entropy shows smooth, nearly sinusoidal oscillations, indicating a controlled and reversible exchange of quantum correlations between the qubit and the field. As the squeezing parameter increases to $r = 1$, additional modulations appear in the entropy evolution; however, the oscillations remain bounded and periodic, reflecting enhanced but still regulated entanglement dynamics. In the strong squeezing regime ($r = 2$), the entropy oscillations become denser and faster, yet their amplitude remains limited compared to the single-photon transition. This demonstrates that two-photon processes effectively suppress excessive decoherence and preserve a higher degree of field purity, even under strong squeezing conditions.

The following schematic qualitatively reproduces the behavior of **Figure 3**, emphasizing the stabilizing role of the two-photon transition on the field purity dynamics:

Interpretation:

- Horizontal axis: scaled time t.
- Vertical axis: linear entropy $\xi_f(t)$.
- Panel (a): $r = 0.5 \rightarrow$ regular, low-frequency oscillations.
- Panel (b): $r = 1 \rightarrow$ modulated but still periodic behavior.
- Panel (c): $r = 2 \rightarrow$ faster oscillations with controlled amplitude.

Figure 4 shows the temporal evolution of field purity for different squeezing parameters, illustrating how qubit-field correlations shape the mixedness of the radiation mode. At early interaction times, the purity exhibits pronounced oscillations, reflecting the rapid exchange of quantum information between the two subsystems. As time progresses, these oscillations become increasingly damped, indicating the gradual buildup of entanglement and irreversible decoherence effects induced by the squeezed reservoir. Notably, stronger squeezing leads to a faster reduction in purity and a lower asymptotic value, demonstrating that nonclassical bath properties significantly enhance the loss of coherence in the field dynamics.

Figure 5 illustrates the temporal evolution of the field purity and its direct correlation with the transient spectral response of the system. At early interaction times, the purity rapidly decreases, indicating the onset of strong qubit–field entanglement driven by the squeezed reservoir. This regime coincides with pronounced spectral broadening and asymmetry, reflecting enhanced quantum correlations and nonclassical fluctuations. As time progresses, purity gradually recovers toward a steady value,

accompanied by a stabilization of the spectral profile. This behavior demonstrates the redistribution of quantum coherence between the qubit and the field and highlights the role of squeezing parameters in controlling decoherence and information exchange dynamics.

5. Conclusion

In this work, we have presented a comprehensive theoretical investigation of the dynamical interaction between a two-level quantum system and a squeezed radiation field, with particular emphasis on transient spectral properties and quantum state purity. By combining an analytical formulation with numerical simulations, the joint qubit–field evolution was accurately characterized beyond stationary and Markovian approximations. The adopted framework enabled a direct connection between the time-dependent emission spectrum and the underlying entanglement and decoherence mechanisms induced by the squeezed reservoir. The results demonstrate that squeezing significantly modifies both the spectral response and the purity dynamics of the field. In the short-time regime, strong nonclassical correlations emerge, manifested through spectral distortion and a rapid reduction of purity, indicating enhanced qubit–field entanglement. This behavior arises from phase-sensitive quantum interference and non-Markovian information backflow, both orchestrated by the squeezed reservoir correlations. The spectral asymmetry is a direct interferometric signature of squeezed-field coupling, while purity oscillations reflect the reversible exchange of quantum information between the system and its engineered environment. As the interaction evolves, coherence redistribution leads to a gradual stabilization of the spectral features and the approach toward a steady mixed state. This interplay highlights the critical role of reservoir engineering in controlling information exchange and decoherence processes in open quantum systems. Overall, the present study provides clear physical insight into the relationship between transient spectral signatures and quantum purity dynamics. The proposed approach offers a versatile platform for analyzing nonclassical light–matter interactions and may serve as a valuable tool for the design of quantum optical devices, quantum communication protocols, and reservoir-controlled quantum technologies. Future extensions of this work may naturally incorporate explicitly non-Markovian dynamics to capture memory effects arising from structured reservoirs and strong system–environment correlations. Such an approach would allow a deeper understanding of information backflow and its direct impact on transient spectral features and purity revivals. Additionally, extending the present framework to the ultra-strong and deep-strong coupling regimes, where the rotating-wave approximation breaks down, would provide access to new dynamical phenomena driven by counter-rotating terms and vacuum-induced processes. From an experimental perspective, the proposed model is well aligned with state-of-the-art platforms such as cavity and circuit quantum electrodynamics, trapped ions, and superconducting qubits, where squeezed fields and time-resolved spectral measurements are increasingly accessible. These extensions would further enhance the relevance of transient spectral analysis as a diagnostic and control tool in emerging quantum technologies.

Author contributions: Conceptualization, LA and CH; validation, LA and CH; formal analysis, LA; investigation, CH; resources, LA and CH; data curation, LA and CH; writing—original draft preparation, LA; writing—review and editing, CH; visualization, LA and CH; supervision, LA and CH; project administration, LA and CH; funding acquisition, LA. All authors have read and agreed to the published version of the manuscript.

Funding: This research was funded by the Deanship of Scientific Research of Taif University, grant number 83/Deanship-of-Scientific-Research and the APC was funded by the Deanship of Scientific Research of Taif University (DSRTU) (https://www.tu.edu.sa/En/Deanships/83/Deanship-of-Scientific-Research).

Institutional review board statement: Not applicable. This study is theoretical and computational in nature, involving no human participants, animals, or biological materials.

Informed consent statement: Not applicable. This study does not involve human subjects.

Data availability statement: The data that support the findings of this study are available from the corresponding author upon reasonable request.

Acknowledgment: The authors would like to acknowledge the Taif University Department of Scientific Research in the Kingdom of Saudi Arabia for assistance and motivation to accomplish the research work.

Conflict of interest: The authors declare no financial conflicts of interest.

AI use statement: AI-based writing assistance was used to enhance the manuscript's language and formatting. The authors confirm that all scientific content and conclusions are original and accurately reflect their work.

Abbreviation

Symbol	**Definition**
N	Average photon number in squeezed reservoir: $N = \sinh^2 r$
M	Two-photon correlation amplitude: $M = \sinh r \cosh r \, e^{i\phi}$
r	Squeezing strength
ϕ	Squeezing phase
$g_k^{(1)}$	One-photon coupling strength
$g_k^{(2)}$	Two-photon coupling strength
κ	Detector bandwidth
$\Gamma_1(t)$	Time-dependent one-photon decay rate
$\Gamma_2(t)$	Time-dependent one-photon excitation rate
$\Gamma_c(t)$	Squeezing-induced correlation rate

References

1. Yang ZB, Yang RC, Liu S. Transmitting squeezed states in a cascaded cavity-magnonic system. Optics Express. 2025; 33(3): 4725. doi: 10.1364/OE.551766
2. Schoelkopf RJ, Girvin SM. Wiring up quantum systems. Nature. 2008; 451(7179): 664–669. doi: 10.1038/451664a
3. Bentley J, Nurdin H, Chen Y, et al. Designing Optimal Linear Detectors: A Bottom-Up Approach. Physical Review

Applied. 2023; 19(3): 034009. doi: 10.1103/PhysRevApplied.19.034009
4. Khalifa M, Feldmann P, Salfi J. Kinetic inductance parametric converter. Physical Review Applied. 2024; 22(2): 024025. doi: 10.1103/PhysRevApplied.22.024025
5. Jacobs K, Krastanov S, Heuck M, et al. Quantum theory of single-photon nonlinearities generated by ensembles of emitters. arXiv preprint. 2023. doi: 10.48550/arXiv.2307.01375
6. Wu Z, Yi Z, Gu W, et al. Enhancement of Optomechanical Squeezing of Light Using the Optical Coherent Feedback. Entropy. 2022; 24(12): 1741. doi: 10.3390/e24121741
7. Yanagimoto R, Ng E, Jankowski M, et al. Mesoscopic ultrafast nonlinear optics—The emergence of multimode quantum non-Gaussian physics. Optica. 2024; 11(7): 896. doi: 10.1364/OPTICA.514075
8. Liu ZX, Zuo XJ, Peng JX, et al. Quantum sensing with cavity optomechanics. Applied Physics Reviews. 2026; 13(1): 011307. doi: 10.1063/5.0237048
9. Molinares H, Eremeev V. Drive-Loss Engineering and Quantum Discord Probing of Synchronized Optomechanical Squeezing. Mathematics. 2025; 13(13): 2171. doi: 10.3390/math13132171
10. Lemieux S, Jalil SA, Purschke DN, et al. Photon bunching in high-harmonic emission controlled by quantum light. Nature Photonics. 2025; 19(7): 767–771. doi: 10.1038/s41566-025-01673-6
11. Yuan M, Seif A, Lingenfelter A, et al. Universal control in bosonic systems with weak Kerr nonlinearities. Physical Review A. 2025; 111(3): 032606. doi: 10.1103/PhysRevA.111.032606
12. González-Madrid JC, Marín LG, Chamorro-Cáceres K, et al. Energy Management System for microgrid operation with green hydrogen storage in the Colombian electricity sector. Journal of Energy Storage. 2026; 152: 120224. doi: 10.1016/j.est.2025.120224
13. Ding Y, Chen X, Magdalena-Benedito R, et al. Closed-loop control of a noisy qubit with reinforcement learning. Machine Learning: Science and Technology. 2023; 4(2): 025020. doi: 10.1088/2632-2153/acd048
14. Barzanjeh S, Xuereb A, Gröblacher S, et al. Optomechanics for quantum technologies. Nature Physics. 2022; 18(1): 15–24. doi: 10.1038/s41567-021-01402-0
15. Al-Sawai WM. Quantum dynamics of a cantilever under combined additive and parametric noise: Implications for squeezing and sensitivity control. Journal of Applied Physics. 2025; 138(16): 164401. doi: 10.1063/5.0291465
16. Wu Y, Xu M, Tang HX. Junction-free microwave two-mode radiation from a kinetic inductance nanowire. Physical Review Applied. 2024; 21(1): 014029. doi: 10.1103/PhysRevApplied.21.014029
17. Wang L, Sun P, Kong LJ, et al. Quantum next-generation reservoir computing and its quantum optical implementation. Physical Review A. 2025; 111(2): 022609. doi: 10.1103/PhysRevA.111.022609
18. Drammeh M, Samikannu R, Yahya A, et al. Optimal energy management system for a community microgrid: A case study from the Gambia. Utilities Policy. 2026; 99: 102132. doi: 10.1016/j.jup.2025.102132
19. Houtepen AJ, Sargent EH, Infante I, et al. Colloidal quantum dots for optoelectronics. Nature Reviews Methods Primers. 2025; 5(1): 42. doi: 10.1038/s43586-025-00413-y
20. Delfanazari K. Chip-scale electrically driven superconducting coherent photon sources for quantum information processing. Nature Photonics. 2025; 19(11): 1163–1177. doi: 10.1038/s41566-025-01735-9
21. Sakurai A, Hayashi A, Munro WJ, et al. Quantum optical reservoir computing powered by boson sampling. Optica Quantum. 2025; 3(3): 238. doi: 10.1364/OPTICAQ.541432
22. Ma J, Yang J, Liu S, et al. Nanophotonic quantum skyrmions enabled by semiconductor cavity quantum electrodynamics. Nature Physics. 2025; 21(9): 1462–1468. doi: 10.1038/s41567-025-02973-y
23. Blais A, Huang RS, Wallraff A, et al. Cavity quantum electrodynamics for superconducting electrical circuits: An architecture for quantum computation. Physical Review A. 2004; 69(6): 062320. doi: 10.1103/PhysRevA.69.062320
24. Yu W, Wang W. Enhancing resilience and cost efficiency in multi-microgrids through peer-to-peer energy trading and decentralized energy management systems. Sustainable Energy, Grids and Networks. 2026; 45: 102116. doi: 10.1016/j.segan.2025.102116
25. Atef M, Alahakoon S, Mumtahina U, et al. A review of microgrid energy management systems: Methods, challenges, and future directions. International Journal of Ambient Energy. 2026; 47(1): 2595117. doi: 10.1080/01430750.2025.2595117